

Peculiarities of the chemical abundance distribution in galaxies NGC 3963 and NGC 7292

A. S. Gusev^{*} and A. V. Dodin

Sternberg Astronomical Institute, Lomonosov Moscow State University, Universitetsky pr. 13, 119234 Moscow, Russia

Accepted 2021 May 11. Received 2021 April 27; in original form 2021 April 24

ABSTRACT

Spectroscopic observations of 32 H II regions in the spiral galaxy NGC 3963 and the barred irregular galaxy NGC 7292 were carried out with the 2.5-m telescope of the Caucasus Mountain Observatory of the Sternberg Astronomical Institute using the Transient Double-beam Spectrograph with a dispersion of $\approx 1 \text{ \AA pixel}^{-1}$ and a spectral resolution of $\approx 3 \text{ \AA}$. These observations were used to estimate the oxygen and nitrogen abundances and the electron temperatures in H II regions through modern strong-line methods. In general, the galaxies have oxygen and nitrogen abundances typical of stellar systems with similar luminosities, sizes, and morphology. However, we have found some peculiarities in chemical abundance distributions in both galaxies. The distorted outer segment of the southern arm of NGC 3963 shows an excess oxygen and nitrogen abundances. Chemical elements abundances in NGC 7292 are constant and do not depend on the galactocentric distance. These peculiarities can be explained in terms of external gas accretion in the case of NGC 3963 and major merging for NGC 7292.

Key words: galaxies: individual: NGC 3963, NGC 7292 – galaxies: abundances – ISM: abundances – H II regions

1 INTRODUCTION

The distribution of chemical elements in galaxies plays a key role in understanding their formation and evolution. Regions of ionized hydrogen with their bright emission spectra are good indicators of this distribution. The oxygen abundance is usually used as a tracer of current metallicity in spiral and irregular galaxies. Numerous spectroscopic observations of H II regions, beginning from [Searle \(1971\)](#), reveal an exponential decrease in the oxygen-to-hydrogen ratio from the centre to the outer disc regions of galaxies.

Chemical elements gradients are the result of the galaxy evolution, where a complex interplay between star formation rate and efficiency, stellar migration, accretion and outflow of metal-poor and metal-rich gas, tidal interactions and mergers, as well as gas flows within the disc form the radial distribution of heavy chemical elements ([Zurita et al. 2021a](#)). The findings of investigations into variations of the gas composition within galaxies, in combination with results on the evolution of stellar populations, has led to the development of models of chemical evolution of galaxies ([Chiappini, Romano & Matteucci 2003](#); [Marcon-Uchida, Matteucci, Costa 2010](#)).

Studies of possible relationships between the abundance properties and global characteristics of galaxies such as morphology and luminosity are equally important ([Pagel 1991](#); [Vila-Costas & Edmunds 1992](#); [Dutil & Roy 1999](#);

[Sánchez et al. 2014](#); [Florido et al. 2015](#); [Pérez-Montero et al. 2016](#); [Zinchenko et al. 2019](#); [Zurita et al. 2021b](#)).

Although the main indicator of metallicity is the oxygen abundance, the nitrogen-to-oxygen ratio plays an equally important role, being an indicator of star formation history ([Mallery et al. 2007](#); [Mollá & Gavilán 2010](#)).

To determine parameters of the oxygen and nitrogen abundance distributions, the abundance estimates for H II regions, evenly distributed across the whole galaxy disc from the inner to the outer part, are necessary. This kind of measurements are available for a few hundred galaxies (see compilations in [Pilyugin, Grebel & Kniazev 2014](#); [Zurita et al. 2021a](#)).

Integral field unit spectroscopy instruments and large surveys, associated with them, provide the most complete data for chemical and kinematic analysis. However, a small field of view of such devices ($74 \times 64 \text{ arcsec}^2$ in CALIFA, for instance) confines the study of giant and nearby galaxies to their inner parts. Wide-field integral spectroscopy instruments provide observational data for smaller number of galaxies. We believe that classical long-slit and multi-slit spectroscopic data still play an important role, especially for studies of some individual galaxies with signs of peculiarity in morphology, which were not included in large spectral surveys.

The newly installed Transient Double-beam Spectrograph (TDS; see Section 2.1 for details) is already used actively in several large international projects such as the SRG/eROSITA All-Sky Survey ([Dodin et al. 2020](#)) and the Zwicky Transient Facility survey ([Malanchev et al. 2021](#)), as well as in various stellar, galactic,

^{*} E-mail: gusev@sai.msu.ru

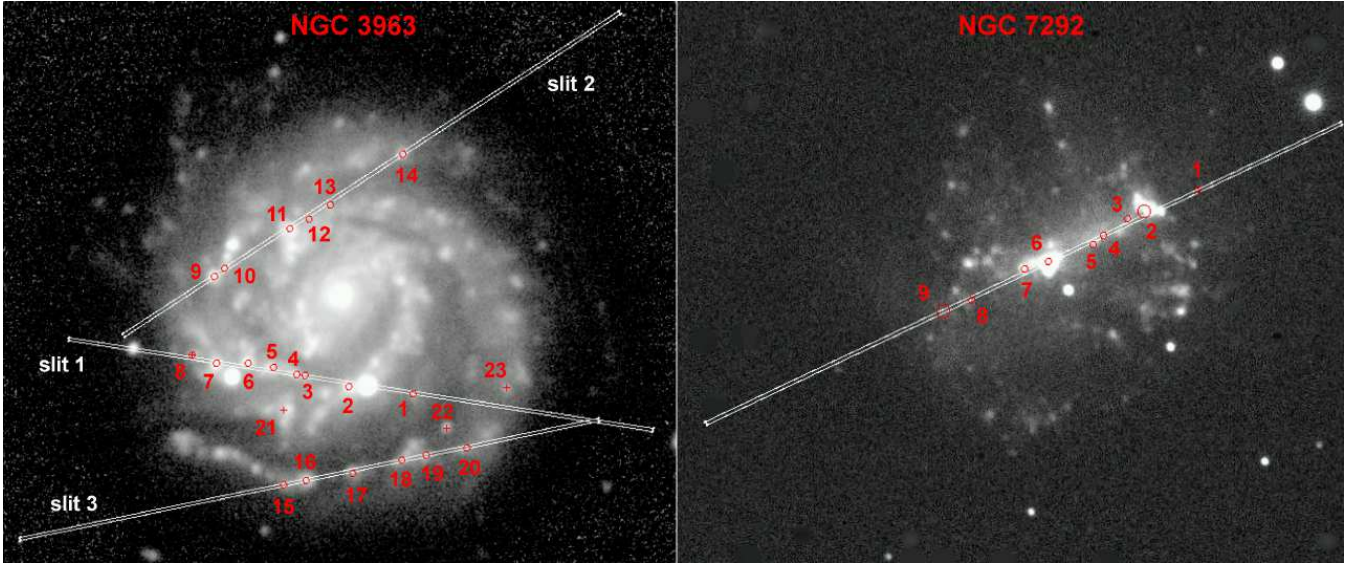


Figure 1. *U* images of NGC 3963 (left) and NGC 7292 (right) with overlaid positions of the slits (white narrow bars). The sizes of the slits are 180×1 arcsec². The positions and numbers of the H II regions observed via TDS (open red circles) and obtained from the SDSS (red crosses) are indicated. The region no. 8 in NGC 3963 (cross in circle) was observed both with the TDS and BOSS (SDSS). North is upwards and east is to the left.

Table 1. The galaxy sample.

| Galaxy | Type | B_i (mag) | M_B^a (mag) | Inclination (degree) | PA (degree) | v^b (km s ⁻¹) | R_{25}^c (arcmin) | R_{25}^c (kpc) | d (Mpc) | $A(B)_{\text{Gal}}$ (mag) | $A(B)_{\text{in}}$ (mag) |
|----------|-----------|------------------|--------------------|-------------------------|----------------|--------------------------------|------------------------|---------------------|--------------|------------------------------|-----------------------------|
| 1 | 2 | 3 | 4 | 5 | 6 | 7 | 8 | 9 | 10 | 11 | 12 |
| NGC 3963 | SAB(rs)bc | 12.60 ± 0.07 | -21.10 ± 0.325 | 28.9 | 95.9 | 3184 | 1.285 | 18.39 | 49.2 | 0.083 | 0.09 |
| NGC 7292 | IBm | 13.06 ± 0.06 | -17.00 ± 1.007 | 54.4 | 113.0 | 986 | 0.953 | 1.89 | 6.82 | 0.223 | 0.32 |

^a Absolute magnitude of a galaxy corrected for Galactic extinction and inclination effects.

^b Heliocentric radial velocity.

^c Radius of a galaxy at the isophotal level 25 mag arcsec⁻² in the *B* band corrected for Galactic extinction and inclination effects.

and extragalactic studies (see [Potanin et al. 2020](#), and references therein). This paper presents the first results of a spectroscopic study of extragalactic H II regions obtained at the TDS.

We selected for spectroscopic study the Milky Way-type galaxy NGC 3963 and NGC 7292 which is similar to Large Magellanic Cloud by size and morphology (Fig. 1, Table 1). Both galaxies host numerous H II regions. NGC 3963 is a rather symmetric grand-design galaxy with distorted outer part of southern spiral arm. It has a companion of comparable mass, NGC 3958, which is located at the distance of 7.7 arcmin (110 kpc) to the south from NGC 3963. Tidal distortions have been found in both galaxies of the pair ([van Moorsel 1983](#)).

NGC 7292 is an irregular galaxy with a strong bright bar. The galaxy looks like a flower with three petals with the bar between two of them (Fig. 1). Let us remark that Magellanic-type galaxies is a rare galactic type. Data on the chemical elements abundance in H II regions in this type of stellar systems are known for a limited number of galaxies (see e.g. [Pilyugin et al. 2014](#), and references therein).

Both galaxies are not isolated and are influenced by the environment: gas accretion in the case of NGC 3963 and a major merging in the case of NGC 7292. The goal of our study is to check how

the environment affects the chemical elements abundance and their spatial distribution in these galaxies.

Spectroscopic observations of H II regions in NGC 3963 and NGC 7292 have not been carried out previously, with the exception of 4 regions, which were observed in the Sloan Digital Sky Survey¹ (SDSS). These regions are included in our study (see Fig. 1).

The fundamental parameters of the galaxies are presented in Table 1, where the morphological type, Galactic absorption, $A(B)_{\text{Gal}}$, and the distance to NGC 3963 are taken from the NED² database, and the remaining parameters are taken from the LEDA³ database. The distance to NGC 7292 is still an open question (see the distance estimates in NED). We use the value of the distance to NGC 7292 obtained in [Tully et al. \(2009\)](#).

¹ <https://www.sdss.org>

² <http://ned.ipac.caltech.edu>

³ <http://leda.univ-lyon1.fr>

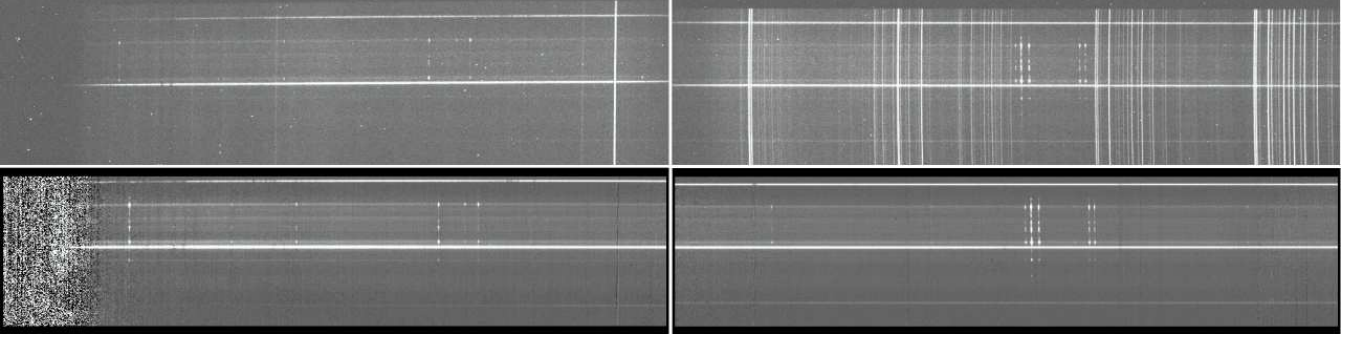


Figure 2. Frames with spectra of NGC 3963 obtained in the position of slit 1 in blue (left panels) and red (right panels) channels of the TDS. The raw spectra (top) and the spectra after initial reduction (bottom) are shown. The sizes of the images are 2048×512 (top) and 2030×460 pixels² (bottom).

Table 2. Journal of observations.

| Slit position | PA _{slit} (degree) | Date | Exposures (s) | Air mass |
|---------------|-----------------------------|---------------|---------------|----------|
| NGC 3963 | | | | |
| 1 | 81.2 | 2020.12.11/12 | 900 × 4 | 1.1 |
| 2 | 123.0 | 2020.12.14/15 | 900 × 3 | 1.6 |
| 3 | 101.7 | 2020.12.17/18 | 900 × 6 | 1.5 |
| NGC 7292 | | | | |
| | 118.3 | 2020.12.10/11 | 100 + 900 × 3 | 1.4 |

2 OBSERVATIONS AND DATA REDUCTION

2.1 Observations

The observations were carried out at the 2.5 m telescope of the Caucasus Mountain Observatory of the Sternberg Astronomical Institute (Lomonosov Moscow State University; CMO SAI MSU) with the TDS. This is a new device which was installed at the end of 2019 (Potanin et al. 2020).

The spectrograph operates simultaneously in blue (the range of $3600\text{--}5770\text{\AA}$ with a dispersion of $1.21\text{\AA pixel}^{-1}$ and a spectral resolution of 3.6\AA) and red (the range of $5673\text{--}7460\text{\AA}$ with a dispersion of $0.87\text{\AA pixel}^{-1}$ and a spectral resolution of 2.6\AA) channels (Potanin et al. 2020). Two CCD cameras use E2V 42-10 detectors with a size of 2048×512 pixels². The pixel size is 0.363 arcsec, the size of slits used is 180×1 arcsec². For a detailed description of the spectrograph, see Potanin et al. (2020).

Observations were carried out in December 2020 (see the journal of observations in Table 2). An example of raw spectrum obtained in both channels is presented in Fig. 2 (top panel).

We chose such slit positions to cover the maximum number of H II regions in a wide range of galactocentric distances. As a result, we obtained spectra for 20 H II regions in NGC 3963 and 9 H II regions in NGC 7292 (Fig. 1).

Spectral data for objects in NGC 3963 were obtained using three slit positions (H II regions nos. 1-8 were covered by the first, nos. 9-14 – by the second, and nos. 15-20 – by the third slit position; see Fig. 1).

Four H II regions in NGC 3963 have been previously observed in the SDSS with the BOSS spectrograph (nos. 8, 21-23). The region no. 8 in NGC 3963 was observed both on the TDS and BOSS

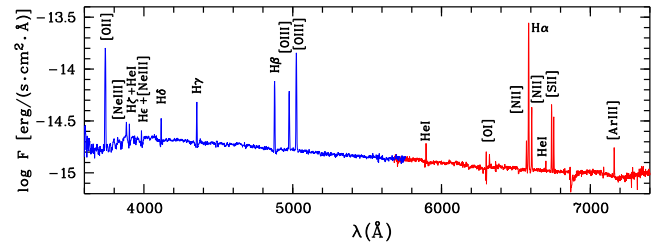


Figure 3. The spectrum of the H II region no. 6 (nucleus) of NGC 7292. The spectra obtained in the blue and red channels of the TDS are overlaid on one another.

(Fig. 1). 1D spectra of these objects⁴ were downloaded from the SDSS DR 16 database.⁵

The seeing during our observations was from 1.2 up to 1.8 arcsec, typical angular diameters of studied H II regions are from 2 up to 7 arcsec (Fig. 1). Remark that the last observational night was cloudy, as a result the spectra obtained in the slit position 3 have a lower signal-to-noise ratio.

The observing procedure involved obtaining flat and wavelength calibration images at the beginning and end of each set. Spectrophotometric standards were observed immediately after the studied objects at the same air mass.

2.2 Data reduction

Initial data reduction followed routine procedures, including dark, cosmic-ray, and flat-field corrections, wavelength calibration with a standard Ne-Al-Si lamp, rebinning the data onto a uniform wavelength grid, wavelength correction using night sky lines, photometric calibration, summation of spectra, subtracting the background, and transformation to one-dimensional spectrum (see Potanin et al. 2020, for details). To reduce raw spectra, we used a PYTHON-based data processing package, developed in SAIMSU, and the European Southern Observatory Munich Image Data Analysis System (ESOMIDAS). An example of final 2D spectrum is presented in Fig. 2 (bot-

⁴ Files: spec-8234-57450-0784.fits (no 8), spec-8237-58162-0466.fits (no 21), spec-8234-57450-0786.fits (no 22), and spec-8237-58162-0462.fits (no. 23)

⁵ <http://skyserver.sdss.org/dr16>

Table 3. Parameters of H II regions, equivalent widths of the H α and H β lines, and underreddened H β line fluxes.

| H II region | N-S ^a (arcsec) | E-W ^a (arcsec) | r^b (kpc) | r/R_{25}^b | $c(\text{H}\beta)$ | n_e (cm ⁻³) | EW(H α) (Å) | EW(H β) (Å) | $F(\text{H}\beta)$ (10 ⁻¹⁶ erg s ⁻¹ cm ⁻²) |
|----------------|---------------------------|---------------------------|-------------|--------------|--------------------|---------------------------|---------------------|--------------------|--|
| NGC 3963 | | | | | | | | | |
| 1 | -30.0 | +22.4 | 9.89 | 0.538 | 1.04 ± 0.15 | < 260 | 94.2 ± 17.1 | 18.7 ± 3.9 | 2.3 ± 0.2 |
| 2 | -27.8 | +2.9 | 7.60 | 0.413 | 0.99 ± 0.02 | < 130 | 185.1 ± 12.7 | 31.2 ± 2.4 | 29.6 ± 0.4 |
| 3 | -24.6 | -10.6 | 7.08 | 0.385 | 1.17 ± 0.08 | < 120 | 105.2 ± 10.4 | 21.5 ± 2.7 | 3.8 ± 0.2 |
| 4 | -24.2 | -13.1 | 7.20 | 0.392 | 0.87 ± 0.03 | < 130 | 155.6 ± 13.9 | 32.2 ± 4.3 | 9.1 ± 0.2 |
| 5 | -22.0 | -20.1 | 7.57 | 0.411 | 0.95 ± 0.08 | < 130 | 70.2 ± 7.6 | 16.0 ± 1.5 | 5.0 ± 0.3 |
| 6 | -20.8 | -28.0 | 8.63 | 0.469 | 1.30 ± 0.27 | 530 ± 220 | 62.0 ± 8.5 | 14.2 ± 1.9 | 1.7 ± 0.2 |
| 7 | -20.8 | -37.5 | 10.46 | 0.569 | 0.92 ± 0.02 | < 60 | 225.5 ± 18.1 | 33.1 ± 2.9 | 25.2 ± 0.3 |
| 8 ^c | -18.2 | -44.8 | 11.67 | 0.635 | 0.83 ± 0.30 | < 110 | 114.1 ± 69.2 | 20.9 ± 12.2 | 0.9 ± 0.2 |
| 8 ^d | -18.2 | -44.8 | 11.67 | 0.635 | - | < 110 | 60.9 ± 22.7 | 17.2 ± 2.5 | 1.8 ± 0.1 |
| 9 | +5.6 | -38.1 | 9.28 | 0.504 | 1.12 ± 0.05 | < 35 | 328.6 ± 112.6 | 42.3 ± 8.7 | 9.6 ± 0.2 |
| 10 | +8.1 | -35.0 | 8.70 | 0.473 | 0.88 ± 0.08 | 360 ± 190 | 217.5 ± 99.8 | 49.0 ± 22.4 | 4.6 ± 0.2 |
| 11 | +20.1 | -15.1 | 6.64 | 0.361 | 2.05 ± 0.55 | < 200 | 46.8 ± 5.4 | 9.8 ± 1.1 | 1.4 ± 0.3 |
| 12 | +23.1 | -9.2 | 6.71 | 0.365 | 1.59 ± 0.52 | < 580 | 61.9 ± 15.0 | 17.1 ± 4.1 | 1.2 ± 0.3 |
| 13 | +27.2 | -2.8 | 7.46 | 0.406 | 1.90 ± 0.92 | < 360 | 63.5 ± 17.7 | 15.7 ± 5.5 | 0.8 ± 0.3 |
| 14 | +43.0 | +19.4 | 12.46 | 0.678 | 1.05 ± 0.12 | < 120 | 214.1 ± 104.6 | 35.5 ± 16.0 | 4.6 ± 0.3 |
| 15 | -57.7 | -17.0 | 16.10 | 0.876 | 1.74 ± 1.37 | < 660 | 60.6 ± 23.1 | 13.3 ± 5.1 | 3.0 ± 1.6 |
| 16 | -56.3 | -10.2 | 15.44 | 0.840 | 2.01 ± 1.84 | < 870 | 46.5 ± 9.9 | 12.2 ± 2.9 | 2.9 ± 1.9 |
| 17 | -54.0 | +4.1 | 14.76 | 0.803 | 1.04 ± 0.10 | < 180 | 187.9 ± 64.2 | 32.3 ± 9.7 | 32.8 ± 1.8 |
| 18 | -50.2 | +18.9 | 14.51 | 0.789 | 0.92 ± 0.09 | < 130 | 125.7 ± 26.6 | 25.3 ± 5.3 | 28.6 ± 1.6 |
| 19 | -48.7 | +26.4 | 14.82 | 0.806 | 0.85 ± 0.14 | < 360 | 90.8 ± 23.3 | 21.7 ± 5.5 | 13.8 ± 1.4 |
| 20 | -46.5 | +38.9 | 15.89 | 0.864 | 1.20 ± 0.19 | < 250 | 67.6 ± 8.9 | 18.6 ± 3.5 | 16.3 ± 1.6 |
| 21 | -35.0 | -16.9 | 10.24 | 0.557 | - | < 110 | 34.4 ± 3.5 | 14.8 ± 1.7 | 1.5 ± 0.2 |
| 22 | -40.4 | +32.5 | 13.64 | 0.742 | - | < 85 | 194.4 ± 28.9 | 55.0 ± 9.3 | 11.0 ± 0.1 |
| 23 | -28.2 | +51.0 | 14.56 | 0.792 | - | < 100 | 39.4 ± 5.7 | 13.5 ± 2.2 | 1.5 ± 0.1 |
| NGC 7292 | | | | | | | | | |
| 1 | +18.5 | +38.6 | 1.42 | 0.750 | 0.84 ± 0.20 | < 120 | 59.3 ± 12.1 | 19.9 ± 5.7 | 2.9 ± 0.4 |
| 2 | +12.9 | +24.7 | 0.93 | 0.490 | 0.68 ± 0.01 | < 40 | 152.9 ± 6.0 | 28.0 ± 1.2 | 108.7 ± 0.9 |
| 3 | +11.0 | +20.3 | 0.77 | 0.407 | 0.78 ± 0.02 | < 65 | 98.9 ± 5.8 | 23.6 ± 1.4 | 31.9 ± 0.6 |
| 4 | +6.7 | +14.3 | 0.52 | 0.277 | 1.12 ± 0.11 | < 40 | 48.9 ± 2.9 | 15.5 ± 1.0 | 9.2 ± 0.6 |
| 5 | +4.5 | +11.5 | 0.41 | 0.217 | 0.63 ± 0.05 | < 45 | 41.3 ± 2.0 | 14.7 ± 0.9 | 10.9 ± 0.6 |
| 6 | 0.0 | 0.0 | 0.00 | 0.000 | 0.57 ± 0.01 | < 60 | 117.3 ± 3.5 | 26.0 ± 0.9 | 226.4 ± 2.0 |
| 7 | -1.8 | -6.1 | 0.21 | 0.113 | 1.03 ± 0.04 | < 20 | 131.8 ± 7.5 | 25.1 ± 2.3 | 42.9 ± 0.9 |
| 8 | -9.7 | -19.5 | 0.72 | 0.382 | 0.98 ± 0.11 | < 30 | 79.1 ± 10.3 | 17.8 ± 2.6 | 9.2 ± 0.7 |
| 9 | -12.8 | -26.9 | 0.99 | 0.522 | 0.62 ± 0.06 | < 20 | 80.9 ± 13.6 | 22.0 ± 3.4 | 12.6 ± 0.7 |

^a Offsets from the galactic centre, positive to the north and west.^b Deprojected galactocentric distance.^c From TDS spectrum.^d From SDSS spectrum.

tom panel). An example of 1D-spectrum after reduction is shown in Fig. 3.

The emission line fluxes were measured using the continuum-subtracted spectrum. Flux calibration was performed, using standard stars BD+75°325, HZ21, and HR4554 from the ESO list.⁶

The extraction aperture corresponded to the area, where the brightest emission lines from H II regions were "visible" above the noise. This size is approximately equal to the angular diameter of individual H II regions projected along the PA of the slit. Thus the apparent sizes of the studied H II regions are larger than the width of the slit.

Coordinates, deprojected galactocentric distances of H II regions, the logarithmic extinction coefficient $c(\text{H}\beta)$, equivalent widths of the H α and H β lines, and underreddened H β line fluxes are listed in Table 3. We also give in this table the electron den-

sities, n_e , of H II regions obtained from the $[\text{S II}]\lambda 6717/[\text{S II}]\lambda 6731$ ratio according to Proxauf, Öttl & Kimeswenger (2014).

When calculating the error of the line flux measurement, we took into account the following factors: the Poisson statistics of the line photon flux, the error connected with the computation of the underlying continuum, and the uncertainty of the spectral sensitivity curve. All these components are summed in quadrature. The total errors have been propagated to calculate the errors of all derived parameters. The use of the 1 arcsec slit introduces an unknown factor up to 2 due to slit losses, which, however, is constant within 3 percent over the spectral range.

The measured emission fluxes F were corrected for the interstellar reddening and Balmer absorption in the underlying stellar continuum. The theoretical H α /H β ratio from Osterbrock (1989), assuming case B recombination and an electron temperature of 10⁴ K and the analytical approximation to the Whitford interstellar reddening law by Izotov, Thuan & Lipovetsky (1994), were used. We adopted the absorption equivalent width of hydrogen lines

⁶ <https://www.eso.org/sci/observing/tools/standards.html>

Table 4. The reddening-corrected fluxes of main emission lines of H II regions in units of $I(H\beta)$.

| H II region | [O II] 3727+3729 | [O III] 4959 | [O III] 5007 | [N II] 6548 | [N II] 6584 | [S II] 6717 | [S II] 6731 |
|-------------|---------------------|-----------------|-----------------|-----------------|-----------------|-----------------|-----------------|
| NGC 3963 | | | | | | | |
| 1 | 5.88 ± 1.10 | 0.17 ± 0.09 | 0.50 ± 0.10 | 0.24 ± 0.05 | 0.78 ± 0.13 | 0.40 ± 0.07 | 0.30 ± 0.06 |
| 2 | 2.21 ± 0.10 | 0.06 ± 0.01 | 0.23 ± 0.01 | 0.30 ± 0.01 | 0.95 ± 0.02 | 0.36 ± 0.01 | 0.27 ± 0.01 |
| 3 | 4.02 ± 0.39 | 0.11 ± 0.04 | 0.33 ± 0.05 | 0.34 ± 0.03 | 1.06 ± 0.09 | 0.42 ± 0.04 | 0.30 ± 0.03 |
| 4 | 2.49 ± 0.13 | 0.10 ± 0.02 | 0.23 ± 0.02 | 0.33 ± 0.01 | 1.03 ± 0.04 | 0.39 ± 0.02 | 0.29 ± 0.01 |
| 5 | 3.36 ± 0.42 | – | 0.17 ± 0.05 | 0.32 ± 0.03 | 0.99 ± 0.09 | 0.49 ± 0.05 | 0.35 ± 0.04 |
| 6 | 8.44 ± 2.43 | – | 0.52 ± 0.13 | 0.28 ± 0.09 | 0.88 ± 0.25 | 0.49 ± 0.15 | 0.51 ± 0.15 |
| 7 | 3.53 ± 0.10 | 0.28 ± 0.02 | 0.78 ± 0.02 | 0.23 ± 0.01 | 0.75 ± 0.02 | 0.42 ± 0.01 | 0.29 ± 0.01 |
| 8 | 7.23 ± 0.55 | 0.13 ± 0.04 | 0.78 ± 0.08 | 0.28 ± 0.03 | 0.82 ± 0.06 | 0.67 ± 0.05 | 0.46 ± 0.04 |
| 9 | 3.03 ± 0.15 | 0.09 ± 0.02 | 0.45 ± 0.02 | 0.32 ± 0.02 | 0.84 ± 0.04 | 0.52 ± 0.03 | 0.34 ± 0.02 |
| 10 | 2.96 ± 0.25 | 0.12 ± 0.04 | 0.35 ± 0.05 | 0.32 ± 0.04 | 0.89 ± 0.08 | 0.36 ± 0.04 | 0.33 ± 0.04 |
| 11 | 14.71 ± 7.55 | – | – | – | 0.95 ± 0.52 | 0.49 ± 0.28 | 0.34 ± 0.20 |
| 12 | 5.49 ± 2.74 | – | – | 0.34 ± 0.18 | 1.07 ± 0.54 | 0.49 ± 0.26 | 0.41 ± 0.22 |
| 14 | 4.50 ± 0.56 | 0.24 ± 0.06 | 0.73 ± 0.08 | 0.30 ± 0.04 | 0.81 ± 0.10 | 0.51 ± 0.07 | 0.34 ± 0.05 |
| 17 | 4.49 ± 0.50 | 0.34 ± 0.06 | 0.70 ± 0.06 | 0.25 ± 0.03 | 0.78 ± 0.08 | 0.56 ± 0.07 | 0.41 ± 0.05 |
| 18 | 5.02 ± 0.49 | 0.37 ± 0.06 | 0.80 ± 0.07 | 0.30 ± 0.03 | 0.80 ± 0.08 | 0.61 ± 0.06 | 0.42 ± 0.05 |
| 19 | 5.01 ± 0.85 | 0.39 ± 0.10 | 0.55 ± 0.11 | 0.35 ± 0.07 | 0.93 ± 0.15 | 0.73 ± 0.13 | 0.60 ± 0.11 |
| 20 | 6.68 ± 1.39 | 0.36 ± 0.12 | 0.85 ± 0.14 | 0.32 ± 0.07 | 0.80 ± 0.15 | 0.52 ± 0.11 | 0.38 ± 0.08 |
| 21 | 7.75 ± 1.18 | – | 0.29 ± 0.09 | 0.30 ± 0.05 | 0.96 ± 0.11 | 0.68 ± 0.09 | 0.44 ± 0.07 |
| 22 | 2.40 ± 0.07 | 0.26 ± 0.01 | 0.74 ± 0.01 | 0.20 ± 0.01 | 0.60 ± 0.01 | 0.32 ± 0.01 | 0.23 ± 0.01 |
| 23 | 6.85 ± 0.79 | 0.31 ± 0.08 | 0.83 ± 0.10 | 0.31 ± 0.08 | 0.94 ± 0.09 | 0.84 ± 0.08 | 0.57 ± 0.06 |
| NGC 7292 | | | | | | | |
| 1 | 10.63 ± 2.43 | 1.37 ± 0.26 | 4.53 ± 0.69 | – | 0.38 ± 0.10 | 0.72 ± 0.17 | 0.46 ± 0.12 |
| 2 | 5.09 ± 0.07 | 0.86 ± 0.01 | 2.55 ± 0.02 | 0.09 ± 0.00 | 0.29 ± 0.00 | 0.42 ± 0.01 | 0.29 ± 0.00 |
| 3 | 5.41 ± 0.16 | 0.74 ± 0.02 | 2.07 ± 0.04 | 0.11 ± 0.01 | 0.42 ± 0.01 | 0.55 ± 0.02 | 0.39 ± 0.01 |
| 4 | 12.46 ± 1.43 | 0.85 ± 0.07 | 2.25 ± 0.16 | 0.18 ± 0.03 | 0.54 ± 0.07 | 0.82 ± 0.10 | 0.55 ± 0.07 |
| 5 | 8.65 ± 0.63 | 0.47 ± 0.05 | 1.47 ± 0.09 | 0.12 ± 0.02 | 0.52 ± 0.04 | 0.75 ± 0.06 | 0.50 ± 0.04 |
| 6 | 4.14 ± 0.05 | 0.70 ± 0.01 | 2.08 ± 0.02 | 0.10 ± 0.00 | 0.32 ± 0.00 | 0.32 ± 0.00 | 0.23 ± 0.00 |
| 7 | 5.80 ± 0.23 | 0.64 ± 0.02 | 2.03 ± 0.05 | 0.12 ± 0.01 | 0.36 ± 0.01 | 0.50 ± 0.02 | 0.32 ± 0.01 |
| 8 | 6.92 ± 0.86 | 0.46 ± 0.06 | 1.50 ± 0.12 | 0.17 ± 0.03 | 0.44 ± 0.06 | 0.67 ± 0.09 | 0.42 ± 0.06 |
| 9 | 5.74 ± 0.48 | 0.71 ± 0.06 | 1.75 ± 0.11 | 0.14 ± 0.03 | 0.42 ± 0.04 | 0.52 ± 0.04 | 0.31 ± 0.03 |

$EW_a(\lambda)=2\text{\AA}$ according to [McCall, Rybski & Shields \(1985\)](#), and $EW_a(\lambda)=0$ for lines other than hydrogen.

Reddening-corrected line intensities $I(\lambda)/I(H\beta)$ are given in Table 4.

3 RESULTS

3.1 Preliminary remarks

As we noted above, the H II region no. 8 in NGC 3963 was observed with both TDS and BOSS. We compared our measurements from the TDS spectrum with results from the BOSS spectrum in Fig. 4. As seen from the figure, the fluxes, obtained from the TDS and BOSS spectra, coincide within the error limits for all main emission lines.

At the same time, the fluxes obtained in the BOSS spectrum, turned out to be 1.9 ± 0.2 times higher than in the TDS spectrum. This is obviously due to the different apertures used. The BOSS has a 3 arcsec round aperture, while on the TDS a 1 arcsec width slit is used.

The measurement errors for emission lines, obtained from the BOSS spectrum, turned out to be significantly smaller than those obtained from the TDS spectrum. This is due to the fact that object no. 8 is one of two faintest objects in our sample, so it has relatively large errors in measured fluxes and $c(H\beta)$ (see Table 4). An additional factor is that the SDSS spectra have already been corrected

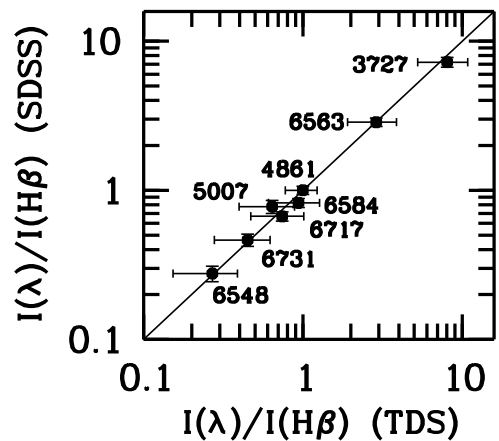


Figure 4. Comparison between reddening-corrected fluxes for the region no 8 in NGC 3963 obtained from the TDS and SDSS spectra. Corresponding wavelengths of spectral lines in \AA are given. The error crosses are shown.

for reddening, so we do not take into account their $c(H\beta)$ errors. Further we will use the results of measurements of the region no. 8 in NGC 3963, obtained from the BOSS spectrum.

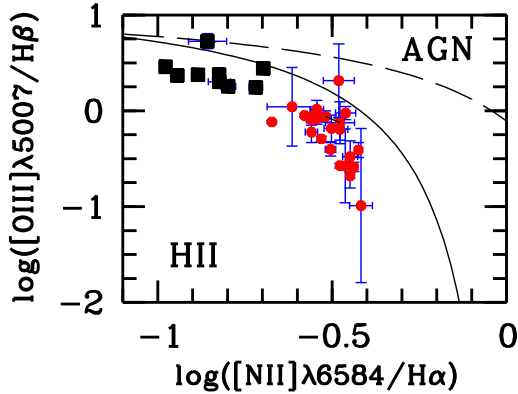


Figure 5. Emission-line diagnostic diagram for H II regions in NGC 3963 (small red circles) and NGC 7292 (large black squares). The curves separate objects with photoionized spectra from the objects with nonthermal emission spectra (AGN) according to Kauffmann et al. (2003) (solid curve) and Kewley et al. (2001) (dashed curve). The error crosses are shown.

As is known, emission spectra can be created by different excitation mechanisms. We examined the studied H II regions on the emission-line diagnostic diagram $[\text{N II}]\lambda 6584/\text{H}\alpha$ versus $[\text{O III}]\lambda 5007/\text{H}\beta$ (Baldwin, Phillips & Terlevich 1981).

Figure 5 shows that most of H II regions from our sample are definitely thermally photoionized objects, that is, classical H II regions. Three regions of our sample (no. 16 in NGC 3963 and nos. 1 and 4 in NGC 7292) are located near the border separating objects with thermal and non-thermal emissions. These objects will be discussed in Section 4.3. Nevertheless, all these H II regions are included in further consideration.

It should be noted that the samples of H II regions in galaxies NGC 3963 and NGC 7292 are located on the diagram in Fig. 5 separately from each other. Objects in NGC 3963 have a systematically lower $[\text{O III}]\lambda 5007/\text{H}\beta$ ratio and a higher $[\text{N II}]\lambda 6584/\text{H}\alpha$ ratio than those in NGC 7292.

We eliminated from further consideration H II regions with large errors in the measured line fluxes. Basically, these errors are the result of large uncertainties in estimates of the extinction coefficient $c(\text{H}\beta)$. The flux measurement errors are comparable to the fluxes themselves for all the main emission lines in regions nos. 13, 15 and 16 in NGC 3963, in which $\Delta c(\text{H}\beta) > 0.9$ (Table 3). These H II regions are not included in Table 4.

Extinction coefficients in H II regions nos. 11 and 12 in NGC 3963 were estimated with errors of > 0.5 (Table 3). As a result, the line fluxes were measured with an accuracy of $\approx 50\%$ (Table 4). Moreover, we were unable to measure $[\text{O III}]\lambda 4959$ and $[\text{O III}]\lambda 5007$ lines for these objects. These two regions were also excluded from further analysis.

3.2 Oxygen and nitrogen abundances

We are unable to use the direct T_e -method to estimate the oxygen and nitrogen abundances, since auroral lines in spectra of H II regions from our sample, such as $[\text{O III}]\lambda 4363$ or $[\text{N II}]\lambda 5755$, are too faint to be detected. Thus, we need to use empirical calibrations. Such methods are well developed (Kobulnicky & Kewley 2004; Pettini & Pagel 2004; Pilyugin & Thuan 2005; Bresolin 2007;

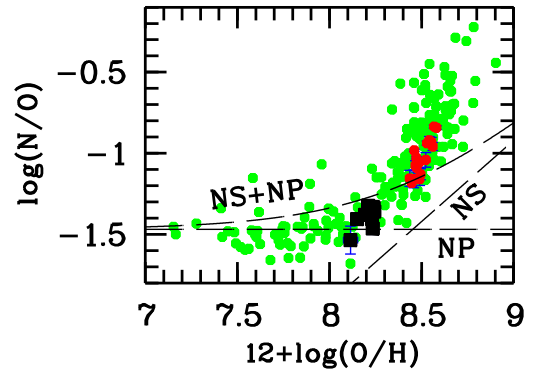


Figure 6. The N/O–O/H diagram for the investigated H II regions in NGC 3963 and NGC 7292. The green circles show T_e -based abundances in the sample of best-studied H II regions in nearby galaxies from the compilation of data of Pilyugin et al. (2010) with additional data from Gusev et al. (2012) and Gusev, Sakhilov & Dodonov (2013). The dashed lines show possible boundaries for data points on the N/O–O/H plane under the assumption of a closed-box model for primary (NP), secondary (NS) and both primary and secondary (NS+NP) nitrogen according to Vila-Costas & Edmunds (1993). Chemical abundances of H II regions of our sample based on R-calibration are shown. Other symbols are the same as in Fig. 5.

Pilyugin, Vílchez & Thuan 2010; Pilyugin & Mattsson 2011; Marino et al. 2013; Pilyugin & Grebel 2016).

The most modern two-dimensional R and S-calibrations (Pilyugin & Grebel 2016) are the simplest and the most popular now. The R-calibration, based on the $[\text{O II}]$ and $[\text{N II}]$ strong emission lines, is more resistant to the presence of diffuse ionized gas (see e.g. Sanders et al. 2017; Kumari et al. 2019; Poetrodjojo et al. 2019), but it is sensitive to extinction errors. The S-method, based on the $[\text{N II}]$ and $[\text{S II}]$ lines, does not depend strongly on extinction, but it can not be used for the nitrogen abundance estimates (Pilyugin & Grebel 2016). Among the other methods we distinguish the NS-calibration (Pilyugin & Mattsson 2011), which is based on the $[\text{O III}]$, $[\text{N II}]$, and $[\text{S II}]$ emission lines intensities (see discussion in Gusev et al. 2012; Gusev, Egorov & Sakhilov 2014).

All the empirical calibrations are constructed under some assumptions. One of them is that the H II regions are in the low-density regime (Pilyugin & Mattsson 2011; Pilyugin & Grebel 2016), which is typical for the majority of extragalactic H II regions (Zaritsky, Kennicutt & Huchra 1994; Bresolin et al. 2005; Gutiérrez & Beckman 2010).

The dependence n_e versus $[\text{S II}]\lambda 6717/[\text{S II}]\lambda 6731$ degenerates at low n_e (Proxauf et al. 2014), thus we give upper limits of n_e in Table 3 for most H II regions. Large upper limits of n_e for H II regions nos. 12, 15, and 16 in NGC 3963 are rather a result of large line flux errors. However, one H II region of our sample, no. 6 in NGC 3963, is an apparently high-density object (see Table 3). The empirical calibrations are not applicable to such regions. As a result, this region was eliminated from further consideration.

We calculated the oxygen and nitrogen abundances in H II regions using three different calibrations discussed above. Data of emission lines fluxes from Table 4 were used. For several regions, where the $[\text{O III}]\lambda 4959$ or $[\text{N II}]\lambda 6548$ lines fluxes have not been measured, we adopt

$$I([\text{O III}]\lambda 4959 + [\text{O III}]\lambda 5007) = 1.33I([\text{O III}]\lambda 5007)$$

and

$$I([\text{N II}]\lambda 6548 + [\text{N II}]\lambda 6584) = 1.33I([\text{N II}]\lambda 6584)$$

according to results of Storey & Zeippen (2000).

The resultant oxygen abundances from the R, NS, and S-calibrations abundances, nitrogen abundances from the R and NS-calibrations, and NS-calibration electron temperatures are given in Table 5.

Chemical elements abundance estimates obtained using various calibrations give small systematic shifts, ~ 0.1 dex for oxygen and ~ 0.15 dex for nitrogen. These are typical shifts between different empirical calibrations (see e.g. Kewley & Ellison 2008; Zurita et al. 2021a, and references therein). Remark that the intrinsic accuracy of strong lines methods is equal to 0.05-0.1 dex (Pilyugin et al. 2010; Pilyugin & Mattsson 2011; Pilyugin & Grebel 2016). These errors are not included in errors in Table 5.

Obtained oxygen and nitrogen abundances and electron temperatures are typical of galaxies with similar luminosities (see e.g. Zurita et al. 2021b). The O/H–N/O diagram (Fig. 6) illustrates this well. All our points lie within the spread of sample of best-studied H II regions in nearby galaxies, where the chemical elements abundances were derived using the direct T_e -method. The diagram shows that NGC 3963 is a system that is rich in oxygen and nitrogen, in which secondary nitrogen dominates. The nitrogen abundance in H II regions of NGC 3963 increases at a faster rate than the oxygen abundance. H II regions in NGC 7292 have lower oxygen abundance and a domination of primary nitrogen (Fig. 6).

3.3 Radial abundance gradients

Radial distributions of oxygen and nitrogen abundances, as well as electron temperatures, obtained using three different calibrations, are presented in Fig. 7.

Both galaxies show a peculiar radial abundance distribution. Both O/H and N/H decrease with distance from the galactic center to distances of $r \approx 0.7R_{25}$ (13 kpc) in NGC 3963 (Fig. 7), which is common for spiral galaxies (Pilyugin et al. 2014). However, we find a flat distribution of oxygen and nitrogen abundances beyond these distances, at $r = 0.7 - 0.9R_{25}$. The flattening of radial oxygen abundance gradients in the outer parts of the discs in some giant galaxies was observed earlier. Ferguson, Gallagher & Wyse (1998) found it in NGC 628 at galactocentric distances $r > R_{25}$. Other similar examples are M83 and NGC 4625 (Pilyugin, Grebel & Mattsson 2012). However, this is a sufficiently rare occurrence. Among a sample of 130 nearby late type galaxies from Pilyugin et al. (2014), we found only three galaxies with the steep inner ($r < 0.7 - 0.8R_{25}$) and flat outer distribution: NGC 1365, NGC 3621, and NGC 5457. All of them have signs of asymmetry in structure.

In the case of NGC 7292, we did not find any significant changes in oxygen and nitrogen abundances with distance from the center (Fig. 7). Only one, the most distant H II region in this galaxy, is distinguished for its lower O/H and N/H abundances.

These peculiarities in chemical abundance distributions in both galaxies will be discussed in Section 4 in more detail.

To estimate radial oxygen and nitrogen abundances gradients, we used standard equations:

$$12 + \log(\text{O}/\text{H}) = 12 + \log(\text{O}/\text{H})_0 + C_{\text{O}/\text{H}}r$$

and

$$12 + \log(\text{N}/\text{H}) = 12 + \log(\text{N}/\text{H})_0 + C_{\text{N}/\text{H}}r,$$

where $12 + \log(\text{O}/\text{H})_0$, $12 + \log(\text{N}/\text{H})_0$ are the extrapolated central oxygen and nitrogen abundances, $C_{\text{O}/\text{H}}$, $C_{\text{N}/\text{H}}$ are the slopes of the oxygen and nitrogen abundances gradients, and r is the galactocentric distance.

The numerical values of the coefficients in the equations have been derived through the least squares method.

For oxygen and nitrogen abundances in NGC 7292 as well as in the outer disc of NGC 3963 ($r \geq 0.7R_{25}$) we give the mean values.

Parameters of radial distributions of oxygen and nitrogen abundances in NGC 3963 and NGC 7292 are presented in Table 6.

Additionally, we calculated the central nitrogen-to-oxygen ratios, $\log(\text{N}/\text{O})_0$, and the slopes of N/O gradient, $C_{\text{N}/\text{O}}$, using the equation

$$\log(\text{N}/\text{O}) = \log(\text{N}/\text{O})_0 + C_{\text{N}/\text{O}}r.$$

Figure 7 and Table 6 show that the radial O/H and N/H gradients, obtained using different calibrations, coincide within slope errors. Both oxygen and nitrogen gradients in the inner part of NGC 3963 are typical for giant spiral galaxies (see e.g. Pilyugin et al. 2014; Zurita et al. 2021b).

Electron temperatures of H II regions anticorrelate with O/H and N/H abundances (Fig. 7). This anticorrelation, indicating that the electron temperature in the nebula essentially depends on the cooling of gas through radiation in the nebular lines, is well known (see the review in Ellison et al. 2008; López-Sánchez & Esteban 2010, for more details). However, it should be noted that O/H, N/H and t_e are dependent parameters in empirical calibrations. Therefore, we can not investigate separately any temperature features in studied H II regions.

4 DISCUSSION

4.1 General chemical distribution parameters

In Fig. 8 we compared general parameters of the chemical elements abundances distribution in NGC 3963 and NGC 7292 (central (mean) O/H and N/O, and their gradients) with similar parameters of galaxies of different luminosity and morphology known from the literature.

Zurita et al. (2021b) found that the O/H and N/O gradients – luminosity relations demonstrate different behaviour for strongly barred and unbarred galaxies; strongly barred galaxies show shallow O/H and N/O gradients, whereas these gradients in unbarred and weakly barred galaxies become steeper as the galactic luminosity decreases.

Inspection of Fig. 8 reveals that both NGC 3963 and NGC 7292 follow well the general trends in the diagrams. The giant weakly barred galaxy NGC 3963 lies within the spread of values of Zurita et al. (2021a) on all diagrams, although it has slightly steeper O/H and N/O gradients (see the filled red circles in Fig. 8). Note, if we take formal results of linear fitting for the full sample of H II regions in NGC 3963 (open red circles in Fig. 8), we will find that the galaxy is not distinguished by central O/H and N/O values and their linear gradients from those of sample of Zurita et al. (2021a).

The strongly barred galaxy NGC 7292 belongs to a rare type of galaxies (see Introduction). Data on the abundance of chemical elements have so far been obtained only for a limited number of Magellanic-type galaxies (see e.g. the sample of Pilyugin et al. (2007) in top-left panel of Fig. 8). Among the galaxies studied by Zurita et al. (2021a), only one galaxy, NGC 4395, is close to NGC 7292 in morphology and luminosity. As seen from Fig. 8,

Table 5. Oxygen and nitrogen abundances and electron temperatures in H II regions derived using the R, NS, and S calibrations.

| H II region Calibration | r/R_{25} | 12+log(O/H) | | | 12+log(N/H) | | T_e NS |
|----------------------------|------------|-------------|-------------|-------------|-------------|-------------|-------------|
| | | R | NS | S | R | NS | |
| NGC 3963 | | | | | | | |
| 1 | 0.538 | 8.44 ± 0.02 | 8.53 ± 0.01 | 8.49 ± 0.02 | 7.28 ± 0.05 | 7.62 ± 0.03 | 0.77 ± 0.02 |
| 2 | 0.413 | 8.57 ± 0.00 | 8.61 ± 0.00 | 8.56 ± 0.00 | 7.73 ± 0.01 | 7.89 ± 0.00 | 0.69 ± 0.01 |
| 3 | 0.385 | 8.56 ± 0.01 | 8.56 ± 0.01 | 8.58 ± 0.01 | 7.60 ± 0.02 | 7.83 ± 0.02 | 0.73 ± 0.02 |
| 4 | 0.392 | 8.58 ± 0.00 | 8.59 ± 0.00 | 8.58 ± 0.00 | 7.74 ± 0.01 | 7.88 ± 0.01 | 0.70 ± 0.01 |
| 5 | 0.411 | 8.55 ± 0.01 | 8.60 ± 0.01 | 8.54 ± 0.01 | 7.62 ± 0.03 | 7.84 ± 0.02 | 0.69 ± 0.03 |
| 7 | 0.569 | 8.47 ± 0.00 | 8.49 ± 0.00 | 8.48 ± 0.00 | 7.44 ± 0.01 | 7.52 ± 0.00 | 0.82 ± 0.00 |
| 8 | 0.635 | 8.45 ± 0.01 | 8.44 ± 0.00 | 8.46 ± 0.01 | 7.26 ± 0.02 | 7.42 ± 0.01 | 0.84 ± 0.01 |
| 9 | 0.504 | 8.53 ± 0.00 | 8.52 ± 0.00 | 8.51 ± 0.01 | 7.59 ± 0.01 | 7.64 ± 0.01 | 0.77 ± 0.01 |
| 10 | 0.473 | 8.54 ± 0.01 | 8.56 ± 0.01 | 8.54 ± 0.01 | 7.62 ± 0.02 | 7.76 ± 0.02 | 0.74 ± 0.01 |
| 14 | 0.678 | 8.49 ± 0.01 | 8.47 ± 0.01 | 8.49 ± 0.02 | 7.43 ± 0.03 | 7.53 ± 0.02 | 0.82 ± 0.01 |
| 17 | 0.803 | 8.47 ± 0.01 | 8.45 ± 0.01 | 8.46 ± 0.01 | 7.39 ± 0.03 | 7.44 ± 0.02 | 0.84 ± 0.01 |
| 18 | 0.789 | 8.47 ± 0.01 | 8.43 ± 0.01 | 8.47 ± 0.01 | 7.38 ± 0.02 | 7.42 ± 0.02 | 0.86 ± 0.01 |
| 19 | 0.806 | 8.52 ± 0.02 | 8.42 ± 0.01 | 8.49 ± 0.02 | 7.48 ± 0.04 | 7.42 ± 0.03 | 0.86 ± 0.01 |
| 20 | 0.864 | 8.46 ± 0.02 | 8.44 ± 0.01 | 8.49 ± 0.02 | 7.30 ± 0.05 | 7.47 ± 0.03 | 0.85 ± 0.01 |
| 21 | 0.557 | 8.49 ± 0.01 | 8.52 ± 0.01 | 8.50 ± 0.02 | 7.33 ± 0.04 | 7.63 ± 0.03 | 0.76 ± 0.03 |
| 22 | 0.742 | 8.46 ± 0.00 | 8.53 ± 0.00 | 8.45 ± 0.00 | 7.48 ± 0.01 | 7.55 ± 0.00 | 0.79 ± 0.00 |
| 23 | 0.792 | 8.50 ± 0.01 | 8.39 ± 0.01 | 8.48 ± 0.02 | 7.37 ± 0.03 | 7.36 ± 0.02 | 0.89 ± 0.01 |
| NGC 7292 | | | | | | | |
| 1 | 0.750 | 8.11 ± 0.04 | 8.30 ± 0.02 | 8.22 ± 0.04 | 6.58 ± 0.08 | 6.82 ± 0.05 | 1.07 ± 0.01 |
| 2 | 0.490 | 8.15 ± 0.00 | 8.26 ± 0.00 | 8.21 ± 0.00 | 6.75 ± 0.00 | 6.84 ± 0.00 | 1.00 ± 0.00 |
| 3 | 0.407 | 8.24 ± 0.00 | 8.31 ± 0.00 | 8.26 ± 0.00 | 6.91 ± 0.01 | 6.91 ± 0.01 | 0.97 ± 0.00 |
| 4 | 0.277 | 8.23 ± 0.02 | 8.36 ± 0.01 | 8.31 ± 0.02 | 6.77 ± 0.03 | 6.96 ± 0.02 | 0.96 ± 0.01 |
| 5 | 0.217 | 8.23 ± 0.01 | 8.32 ± 0.01 | 8.28 ± 0.01 | 6.83 ± 0.02 | 6.90 ± 0.01 | 0.93 ± 0.00 |
| 6 | 0.000 | 8.21 ± 0.00 | 8.31 ± 0.00 | 8.27 ± 0.00 | 6.89 ± 0.00 | 6.97 ± 0.00 | 0.95 ± 0.00 |
| 7 | 0.113 | 8.19 ± 0.00 | 8.30 ± 0.00 | 8.25 ± 0.01 | 6.81 ± 0.01 | 6.90 ± 0.01 | 0.96 ± 0.00 |
| 8 | 0.382 | 8.24 ± 0.01 | 8.32 ± 0.01 | 8.28 ± 0.02 | 6.89 ± 0.03 | 6.92 ± 0.02 | 0.93 ± 0.01 |
| 9 | 0.522 | 8.24 ± 0.01 | 8.33 ± 0.01 | 8.29 ± 0.01 | 6.91 ± 0.03 | 6.98 ± 0.02 | 0.94 ± 0.01 |

Table 6. Parameters of radial distributions of oxygen and nitrogen abundances in the galaxies.

| Calibration | 12 + log(O/H) | | | 12 + log(N/H) | | |
|---------------------------------|---------------|----------------------------------|--------------------------------|---------------|----------------------------------|--------------------------------|
| | centre | gradient (dex R_{25}^{-1}) | gradient (dex kpc $^{-1}$) | centre | gradient (dex R_{25}^{-1}) | gradient (dex kpc $^{-1}$) |
| NGC 3963 ($r < 0.7R_{25}$) | | | | | | |
| R | 8.73 ± 0.09 | -0.43 ± 0.09 | -0.023 ± 0.005 | 8.22 ± 0.18 | -1.39 ± 0.35 | -0.076 ± 0.019 |
| NS | 8.78 ± 0.04 | -0.49 ± 0.07 | -0.027 ± 0.004 | 8.45 ± 0.09 | -1.51 ± 0.18 | -0.082 ± 0.010 |
| S | 8.71 ± 0.03 | -0.37 ± 0.06 | -0.020 ± 0.003 | – | – | – |
| NGC 3963 ($r \geq 0.7R_{25}$) | | | | | | |
| R | 8.48 ± 0.03 | 0 | 0 | 7.40 ± 0.07 | 0 | 0 |
| NS | 8.44 ± 0.05 | 0 | 0 | 7.44 ± 0.06 | 0 | 0 |
| S | 8.47 ± 0.02 | 0 | 0 | – | – | – |
| NGC 7292 | | | | | | |
| R | 8.21 ± 0.05 | 0 | 0 | 6.81 ± 0.11 | 0 | 0 |
| NS | 8.31 ± 0.03 | 0 | 0 | 6.91 ± 0.06 | 0 | 0 |
| S | 8.26 ± 0.03 | 0 | – | – | – | – |

NGC 7272 and NGC 4395 have similar central oxygen abundances, central oxygen-to-nitrogen ratios, as well as O/H and N/O gradients.

4.2 NGC 3963 features

In spite of ordinary general chemical parameters, H II regions in the outer disc of NGC 3963 show the same oxygen and nitrogen abundances within the accuracy of the R-calibration independently of their galactocentric distance (Fig. 7, see also the middle part of

Table 6). Moreover, their O/H and N/H abundances, and N/O ratio seem to be slightly higher than those in H II regions from the middle part ($r \approx 0.55R_{25}$) of the NGC 3963 disc. All these H II regions (nos. 17-20, 22, 23) are located in the southern and south-western parts of NGC 3963 (Fig. 1). The deprojected linear distance between the outermost regions (nos. 17 and 23) is 13 kpc. Recall that the objects nos. 17-20 were observed using TDS (slit position 3) while the regions nos. 22, 23 were observed using BOSS, i.e. in two independent projects.

As we noted in the Introduction, NGC 3963 has a compan-

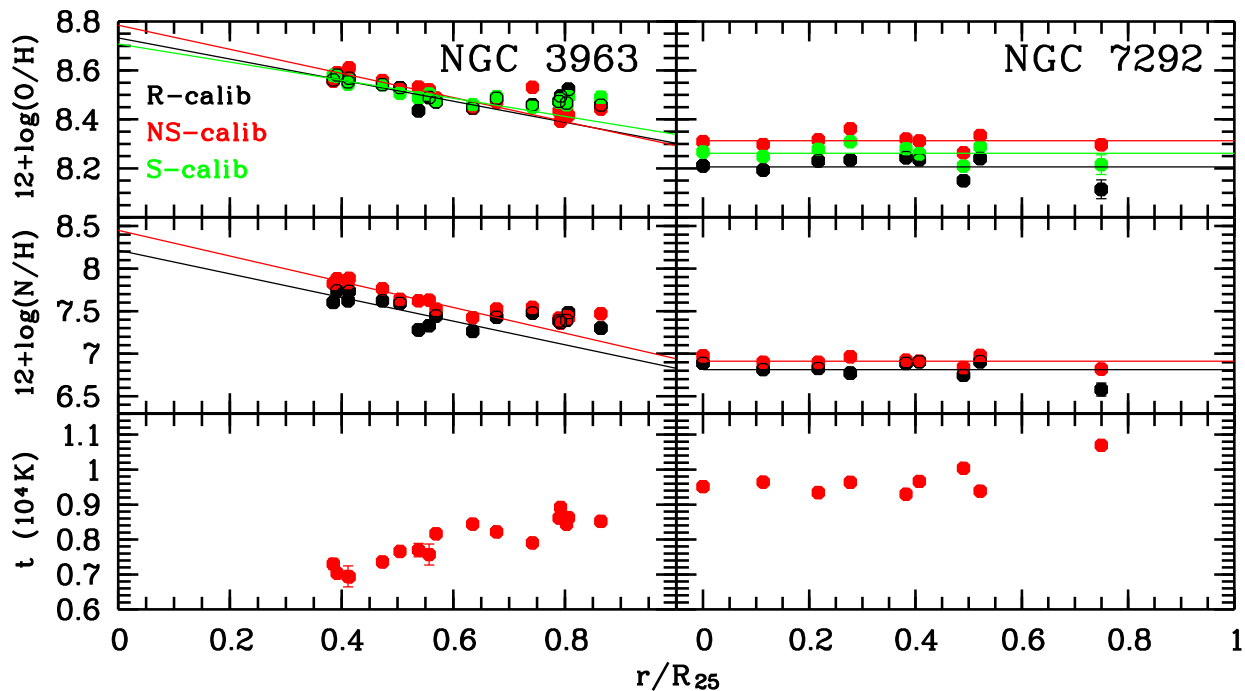


Figure 7. Radial distributions of oxygen abundances (top panels), nitrogen abundances (middle panels), and electron temperatures (bottom panels) in NGC 3963 (left) and NGC 7292 (right) calculated using R- (black), NS- (red), and S-calibrations (green). The solid lines are the best fits to data for NGC 3963 at $r < 0.7R_{25}$ and NGC 7292. The error bars are shown. See the text for details.

ion, NGC 3958, which is located at the distance of 110 kpc from NGC 3963 in the SSW direction. This pair has been repeatedly studied in the 21 cm line (van Moorsel 1983; Nordgren et al. 1997). Results of H I data analysis strongly suggest the presence of tidal distortion in both galaxies in the pair (van Moorsel 1983). Actually, features of the H I spatial distribution and the H I velocity field in NGC 3963 can be clearly interpreted as the presence of a powerful gas inflow from the south-western direction (see H I maps and velocity fields for NGC 3963 in van Moorsel 1983; Nordgren et al. 1997). This flow shoves gas behind the nucleus into the north-eastern part of the galaxy.

We assume that the inflow of metal-enriched gas into the south-western part of the galaxy can stimulate star formation in the southern and south-western parts of the outer disc of NGC 3963. As a result, we observe H II regions with the same, comparatively rich chemical abundance. It is possible that this stream is also responsible for the distortion of the southern spiral arm from the form of the classical logarithmic spiral (see Fig. 1).

We do not discuss H II region no. 14 with $r = 0.68R_{25}$, which is located at the end of the northern spiral arm of NGC 3963 (Fig. 1). It has intermediate O/H and N/H abundances between the regions in the inner and the outer discs (Fig. 7), but we have not any other spectral data for H II regions in the outer disc in the northern part of NGC 3963.

4.3 NGC 7292 features

Oxygen and nitrogen abundances usually do not decrease with galactocentric distance in dwarf and irregular galaxies (Richer & McCall 1995; Miller 1996; Pilyugin 2001; Hidalgo-Gómez, Olofsson & Masegosa 2001; Testor 2001;

Testor, Lemaire & Field 2003; Peimbert, Peimbert & Ruiz 2005; Hernández-Martínez et al. 2009). NGC 7292 is a good example of an irregular galaxy without radial abundance gradient. However, the chemical elements abundance distribution in NGC 7292 is neither strongly constant nor chaotic.

We noted in Section 3.1 H II regions nos. 1 and 4 which are located near the border separating objects with thermal and non-thermal emissions on the $[\text{N II}]\lambda 6584/\text{H}\alpha$ versus $[\text{O III}]\lambda 5007/\text{H}\beta$ diagnostic diagram (Fig. 5). Both these regions stand out in the $\log R_{23}$ –O/H diagram (Fig. 9) too.

This diagram, where

$$R_{23} = I([\text{O II}]\lambda 3727 + 3729 + [\text{O III}]\lambda 4959 + [\text{O III}]\lambda 5007) / I(\text{H}\beta),$$

separates cool rich-oxygen and hot low-oxygen H II regions (see e.g. Pilyugin et al. 2010). If the objects from NGC 3963 occupy the area, where cool rich-oxygen regions, typical for giant galaxies, are located, while most objects from NGC 7292 occupy the area, where warm moderate-metallicity H II regions are located, then regions nos. 1 and 4 from NGC 7292 show extremely high R_{23} for any O/H (Fig. 9). This indicates a significant role of the non-thermal (shock) emission in the formation of spectra of these H II regions. Regions nos. 1 and 4 are also distinguished by the maximum errors in O/H, N/H, and N/O estimates and the largest differences between O/H, N/H, and N/O values calculated using different calibrations (see Figs. 7, 10, Table 5). It is interesting that the region no. 4 is located in the centre of the bar of NGC 7292 at 500 pc from the nucleus and the faint region no. 1 is located in the outer western part of the galaxy (Fig. 1).

We have considered the O/H, N/O, and $\log R_{23}$ distributions along the bar (and the major axis) of NGC 7292 in Fig. 10.

The nucleus (the region no. 6) of NGC 7292 shows the highest

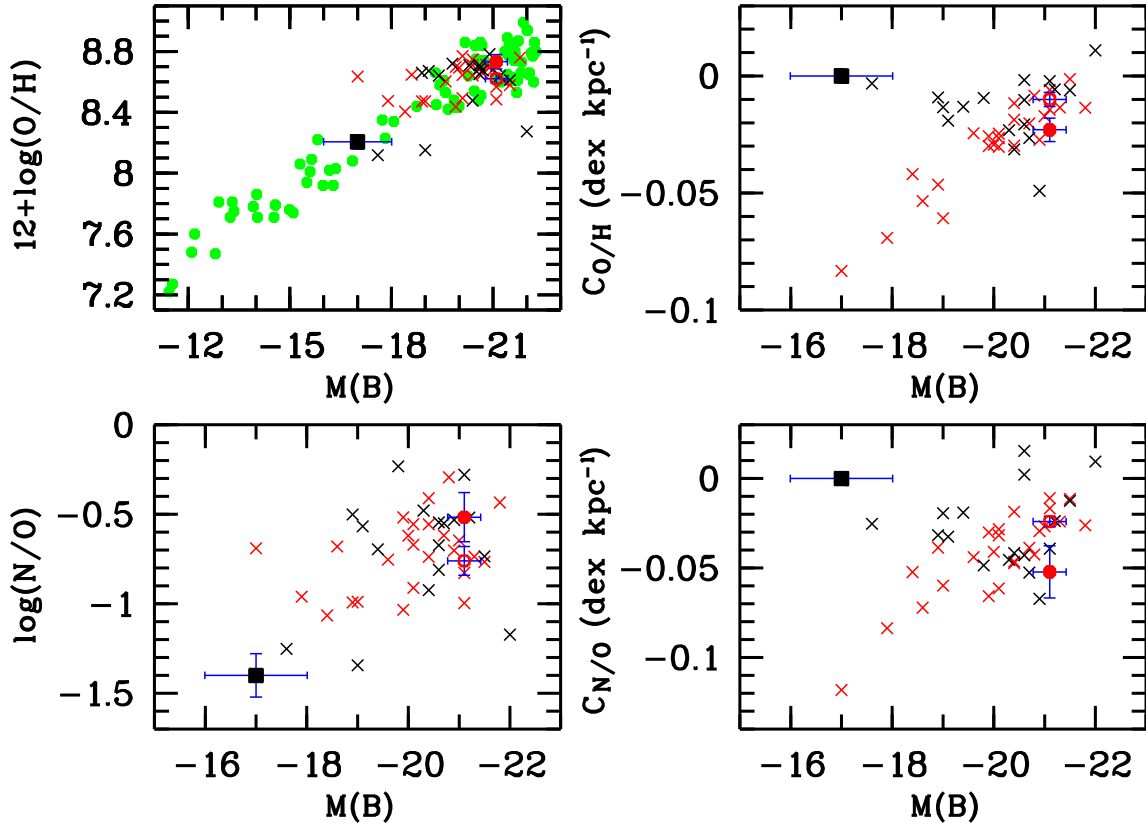


Figure 8. Central (mean) O/H and N/O and their gradients for galaxies of different luminosity. The green circles denote the central oxygen abundances in the discs of spiral galaxies and the oxygen abundances in irregular galaxies from Pilyugin et al. (2007) with additional data from Gusev et al. (2012) and Gusev et al. (2013). The crosses indicate the parameters of strongly barred (black) and unbarred and weakly barred galaxies from Zurita et al. (2021a) obtained using the R-calibration. The filled red circle shows the parameters derived for H II regions sample in the inner disc of NGC 3963 ($r < 0.7R_{25}$), the open red circle denotes the parameters of fitting of full sample of H II regions in NGC 3963, and the black square indicate the mean parameters of chemical abundance distribution in NGC 7292 calculated using the R-calibration. The error crosses are shown. See the text for details.

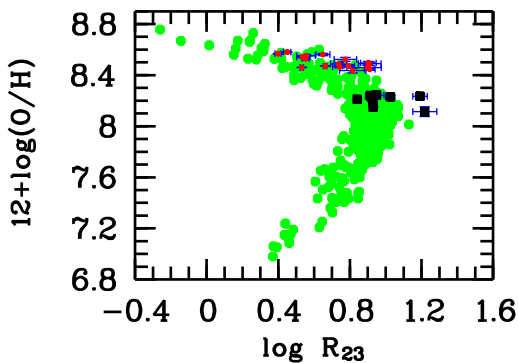


Figure 9. The $\log R_{23}$ –O/H diagram for the sample of H II regions investigated in the present study (symbols are the same as in Fig. 5) and taken from the literature (Pilyugin et al. 2012; Gusev et al. 2012, 2013).

N/O ratio among H II regions in the galaxy. The second by brightness region no. 2 (the end of the bar; see Fig. 1) has minimum oxygen abundance and low N/O ratio (Fig. 10). In general, we observe a weak N/O gradient along the major axis of NGC 7292: the N/O

ratio decreases from the eastern to the western part of the galaxy (see the middle panel in Fig. 10).

Higher values of N/O correspond to smaller specific star formation rate within an H II region, i.e. star formation in it could have been high in the past, at earlier stage of evolution (Mallery et al. 2007; Mollá & Gavilán 2010). The lower N/O ratios correspond to younger, less evolved H II regions. Thus, the observed N/O gradient may indicate the propagation of a star formation wave along the major axis of NGC 7292 from the east to the west of the galaxy. Unfortunately, the absence of H I and H II velocity fields makes it impossible to develop our hypothesis without additional observational data.

5 CONCLUSIONS

The spectroscopic observations of 32 H II regions in NGC 3963 and NGC 7292, obtained with the 2.5-m telescope of the Caucasus Mountain Observatory of the Sternberg Astronomical Institute with the newly Transient Double-beam Spectrograph, were carried out.

The oxygen and nitrogen abundances in 26 H II regions are estimated using different empirical calibrations. Parameters of radial

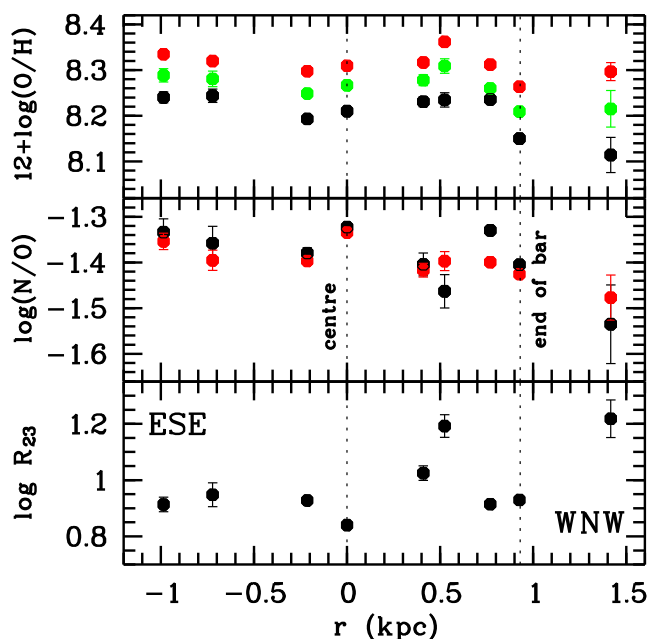


Figure 10. Distributions of oxygen abundance (top), nitrogen-to-oxygen ratio (middle), and $\log R_{23}$ (bottom) along the bar of NGC 7292. Symbols are the same as in Fig. 7. The centre and the end of the bar of the galaxy are indicated by dotted lines. See the text for details.

distributions of the oxygen and nitrogen abundances in the galaxies are obtained. The chemical elements abundance data for H II regions in NGC 3963 and NGC 7292 are estimated for the first time.

General chemical elements abundances and their distribution in NGC 3963 and NGC 7292 are typical for galaxies with similar luminosities and morphology. Wherein, both galaxies have some peculiarities in chemical abundance distributions.

H II regions in the outer part of southern spiral arm of NGC 3963 at distances $r > 0.7R_{25}$ show constant, slightly higher oxygen and nitrogen abundances. This can be explained by the inflow of metal-enriched gas into the south-western part of NGC 3963.

Oxygen and nitrogen abundances do not decrease with galactocentric distance in NGC 7292. However, the nitrogen-to-oxygen ratio seems to decrease along the major axis from the eastern to the western part of the galaxy.

ACKNOWLEDGMENTS

We are grateful to M. A. Burlak (SAI MSU) for help and support during the observations, to O. V. Egorov (Astronomisches Rechen-Institut, Universität Heidelberg and SAI MSU) for helpful comments on different empirical calibrations, and to E. V. Shimanovskaya (SAI MSU) for help with editing this paper. This study was supported by the Russian Foundation for Basic Research (project no 20-02-00080). AVD acknowledges the support by the Interdisciplinary Scientific and Educational School of Moscow University "Fundamental and Applied Space Research". The authors acknowledge support from M.V. Lomonosov Moscow State University Program of Development in expanding the instrumentation base of the CMO SAI MSU. The authors acknowledge the use of the HyperLeda data

base (<http://leda.univ-lyon1.fr>), the NASA/IPAC Extragalactic Database (<http://ned.ipac.caltech.edu>), and The Sloan Digital Sky Survey (<http://www.sdss.org>).

DATA AVAILABILITY

The SDSS data used in this article are available in the SDSS-DR16 database at <http://skyserver.sdss.org/dr16/>. The TDS spectroscopic data can be shared on reasonable request to the corresponding author.

REFERENCES

- Baldwin J. A., Phillips M. M., Terlevich R., 1981, *PASP*, 93, 5
 Bresolin F., 2007, *ApJ*, 656, 186
 Bresolin F., Schaerer D., Conzález Delgado R. M., Stasińska G., 2005, *A&A*, 441, 981
 Chiappini V., Romano D., Matteucci F., 2003, *MNRAS*, 339, 63
 Dodin A. V. et al., 2020, *Astron. Lett.*, 46, 429
 Dutil D. R., Roy J.-R., 1999, *ApJ*, 516, 62
 Ellison S. L., Patton D. R., Simard L., McConnachie A. W., 2008, *AJ*, 135, 1877
 Ferguson A. M. N., Gallagher J. S., Wyse R. F. G., 1998, *AJ*, 116, 673
 Florido E., Zurita A., Pérez I., Pérez-Montero E., Coelho P. R. T., Gadotti D. A., 2015, *A&A*, 584, id. A88
 Gusev A. S., Pilyugin L. S., Sakhibov F., Dodonov S. N., Ezhkova O. V., Khramtsova M. S., 2012, *MNRAS*, 424, 1930
 Gusev A. S., Sakhibov F. H., Dodonov S. N., 2013, *Astr. Bull.*, 68, 40
 Gusev A. S., Egorov O. V., Sakhibov F., 2014, *MNRAS*, 437, 1337
 Gutiérrez L., Beckman J. E., 2010, *ApJ*, 710, L44
 Hernández-Martínez L., Peña M., Carigi L., García-Rojas J., 2009, *A&A*, 505, 1027
 Hidalgo-Gómez A. M., Olofsson K., Masegosa J., 2001, *A&A*, 367, 388
 Izotov Y. I., Thuan T. X., Lipovetsky V. A., 1994, *ApJ*, 435, 647
 Kauffmann G. et al., 2003, *MNRAS*, 346, 1055
 Kewley L. J., Ellison S. L., 2008, *ApJ*, 681, 1183
 Kewley L. J., Dopita M. A., Sutherland R. S., Heisler C. A., Trevena J., 2001, *ApJ*, 556, 121
 Kobulnicky H. A., Kewley L. J., 2004, *ApJ*, 617, 240
 Kumari N., Maiolino R., Belfiore F., Curti M., 2019, *MNRAS*, 485, 367
 López-Sánchez Á. R., Esteban C., 2010, *A&A*, 517, id. A85
 Malanchem K. L. et al., 2021, *MNRAS*, 502, 5147
 Mallery R. P. et al., 2007, *ApJS*, 173, 482
 Marcon-Uchida M. M., Matteucci F., Costa R. D. D., 2010, *A&A*, 520, id. A35
 Marino R. A. et al., 2013, *A&A*, 559, id. A114
 McCall M. L., Rybski P. M., Shields G. A., 1985, *ApJS*, 57, 1
 Miller B. W., 1996, *AJ*, 112, 991
 Mollá M., Gavilán M., 2010, *Mem. Soc. Astron. It.*, 81, 992
 Nordgren T. E., Chengalur J. N., Salpeter E. E., Terzian Y., 1997, *AJ*, 114, 77
 Osterbrock D.E., 1989, *Astrophysics of Gaseous Nebulae and Active Galactic Nuclei*. University Science Books, Mill Valley, CA, p. 422
 Pagel B. E. J., 1991, in Oberhummer H., ed., *Nuclei in the Cosmos*. Springer, Berlin, p. 89
 Peimbert A., Peimbert M., Ruiz M. T., 2005, *ApJ*, 634, 1056
 Pettini M., Pagel B., 2004, *MNRAS*, 348, L59
 Pilyugin L. S., 2001, *A&A*, 374, 412
 Pilyugin L. S., Grebel E. K., 2016, *MNRAS*, 457, 3678
 Pilyugin L. S., Mattsson L., 2011, *MNRAS*, 412, 1145
 Pilyugin L. S., Thuan T. X., 2005, *ApJ*, 631, 231
 Pilyugin L. S., Thuan T. X., Vílchez J. M., 2007, *MNRAS*, 376, 353
 Pilyugin L. S., Vílchez J. M., Thuan T. X., 2010, *ApJ*, 720, 1738
 Pilyugin L. S., Grebel E. K., Mattsson L., 2012, *MNRAS*, 424, 2316
 Pilyugin L. S., Grebel E. K., Kniazev A. Y., 2014, *AJ*, 147, id. A131

- Poetrodjojo H., D'Agostino J. J., Groves B., Kewley L., Ho I.-T., Rich J., Madore B. F., Seibert M., 2019, *MNRAS*, 487, 79
- Potantin S. A. et al., 2020, *Astron. Lett.*, 46, 836
- Proxauf B., Öttl S., Kimeswenger S., 2014, *A&A*, 561, id. A10
- Pérez-Montero E. et al., 2016, *A&A*, 595, id. A62
- Richer M. G., McCall M. L., 1995, *ApJ*, 445, 642
- Sanders R. L., Shapley A. E., Zhang K., Yan R., 2017, *ApJ*, 850, id. 136
- Searle L., 1971, *ApJ*, 168, 327
- Storey P. J., Zeppen C. J., 2000, *MNRAS*, 312, 813
- Sánchez S. F. et al., 2014, *A&A*, 563, id. A49
- Testor G., 2001, *A&A*, 372, 667
- Testor G., Lemaire J. L., Field D., 2003, *A&A*, 407, 905
- Tully R. B., Rizzi L., Shaya E. J., Courtois H. M., Makarov D. I., Jacobs B. A., 2009, *AJ*, 138, 323
- van Moorsel G. A., 1983, *A&AS*, 53, 271
- Vila-Costas M. B., Edmunds M. G., 1992, *MNRAS*, 259, 121
- Vila-Costas M. B., Edmunds M. G., 1993, *MNRAS*, 265, 212
- Zaritsky D., Kennicutt R. C., Huchra J. P., 1994, *ApJ*, 420, 87
- Zinchenko I. A., Just A., Pilyugin L. S., Lara-Lopez M. A., 2019, *A&A*, 623, id. A7
- Zurita A., Florido E., Bresolin F., Pérez-Montero E., Pérez I., 2021a, *MNRAS*, 500, 2359
- Zurita A., Florido E., Bresolin F., Pérez I., Pérez-Montero E., 2021b, *MNRAS*, 500, 2380